2009

Effects of Discrete-Electrode Configuration on Traveling-Wave Electrohydrodynamic Pumping

B D. Iverson

L Cremaschi

S V. Garimella
Purdue University, sureshg@purdue.edu

Iverson, B D.; Cremaschi, L; and Garimella, S V., "Effects of Discrete-Electrode Configuration on Traveling-Wave Electrohydrodynamic Pumping" (2009). *CTRC Research Publications.* Paper 112.
http://dx.doi.org/10.1007/s10404-008-0317-1

Effects of discrete-electrode configuration on traveling-wave electrohydrodynamic pumping

Brian D. Iverson[a], Lorenzo Cremaschi[b] and Suresh V. Garimella[a]

[a]NSF Cooling Technologies Research Center
School of Mechanical Engineering and Birck Nanotechnology Center
Purdue University
585 Purdue Mall
West Lafayette, Indiana 47907-2088
Email: sureshg@purdue.edu

[b]School of Mechanical and Aerospace Engineering
Oklahoma State University
218 Engineering North
Stillwater, OK 74078

ABSTRACT

Traveling-wave electrohydrodynamic (EHD) micropumps can be incorporated into the package of an integrated circuit chip to provide active cooling. They can also be used for fluid delivery in microdevices. The pump operates in the presence of a thermal gradient through the fluid layer such that a gradient in electrical conductivity is established allowing ions to be induced. These ions are driven by a traveling electric field. Such a traveling electric field can be realized in practice only via discrete electrodes upon which the required voltages are imposed. The impact of using discrete electrodes to create the traveling wave on the flow rates generated is explored through numerical modeling. The change in performance from an ideal sinusoidal voltage boundary condition is quantified. The model is used to explore the widths of electrodes and the intervening isolation regions that lead to optimized pumping. The influence of the choice of working fluid on the performance of the pump is determined using an analytical model.

KEYWORDS:

electrohydrodynamics, micropump, microfluidics, fluid delivery, electronics cooling

1. INTRODUCTION

Thermal management of electronic components is of increasing concern in the development of reliable and portable electronic devices. The need to reduce package weight and volume while increasing the functionality has been widely discussed in recent years. The reduction in transistor size and the increase in power density necessitate alternative cooling techniques to replace conventional air-cooled heat sinks. Among the alternative strategies for improved thermal management of electronic systems, liquid cooling using microchannels offers the ability to increase power dissipation while also maintaining a small form factor. Contact and spreading resistances can be reduced or even eliminated by integrating the channels directly on the back side of common flip-chip designs. Further, by using liquid cooling, the heat-generation and heat-dissipation components can be separated, allowing the convective surface area to be unconstrained by the microprocessor area (Mahajan et al. 2006). Thus, the heat exchanger in the cooling loop can be placed at any convenient location in the system. Typically, desirable attributes of a pump for electronics cooling are that they provide high flow rates with low power consumption. However, high flow rates usually translate to large pumps to drive the liquid flow. The prohibitive pumping requirements have limited the application of microchannel heat sinks in space-constrained electronics (Garimella et al. 2006). Solutions which integrate micropumps directly into the microchannels thus represent an important research area to facilitate broader use of liquid cooling in electronic systems.

Additionally, the development of cell analysis tools has recently targeted microfluidic devices since they can be used to sample, trap, separate, sort, treat and analyze cells (Andersson and Van den Berg 2003). Microfluidic devices offer many attractive benefits for biological handling and analysis. For example, reducing device size also reduces sample requirements and reagent volumes, which can reduce overall cost. Test chips are often disposable which is important for sterility. Using microfluidic chips also allows for a closed system, thus protecting the operator from chemical exposure. The small size accommodates parallel operations and thereby reduces cell sorting, analysis and treatment times. Combining different functions on a single microchip is another step toward achieving a completely closed system that can be fully

automated, reduce contamination, and eliminate human intervention and error (Wolff et al. 2003). However, for microfluidic devices to capitalize on all of the above benefits, integration of the fluid pumping mechanism is imperative. Early microfabricated cell-sorting devices used electroosmotic flow as the driving mechanism, which resulted in low sample throughput (Fu et al. 1999). An increased throughput has been achieved using pressure-driven alternatives, but at the expense of removing the pumping mechanism from the chip level (Fu et al. 2002, Wolff et al. 2003). Regardless, the target flow rates for pumping biological materials are typically much lower than for convective cooling, allowing reduced demands on pump operating conditions (such as voltage, power, etc.) to obtain the desired range of fluid flow.

Recent reviews of possible micropumping mechanisms are available in (Iverson and Garimella 2008, Laser and Santiago 2004, Singhal et al. 2004). Although electrohydrodynamics (EHD) has been studied for many years (Melcher 1966, Melcher and Firebaugh 1967, Seyed-Yagoobi 2005, Seyed-Yagoobi et al. 1989a, Seyed-Yagoobi et al. 1989b), it has recently emerged as a potential driving mechanism for micropumps due to its miniaturization potential (Choi and Kim 1995, Fuhr et al. 1992). Further, EHD pumps have the ability to pump a variety of liquids for applications in various research fields (Crowley et al. 1990). A particular advantage of these pumps is that for traveling-wave induction EHD pumps, no modifications are necessary to enable pumping of different types of liquids other than a change in frequency of excitation (Fuhr et al. 1994).

Melcher and Firebaugh (Melcher and Firebaugh 1967), in an early EHD model, used the electric shear approach to calculate the flow profile due to induction EHD. This analytical solution neglected the time and space variation in induced charge density and assumed quasi-static flow. Later models have considered a similar approach using the electric shear stress but have considered developing flow as well (Seyed-Yagoobi et al. 1989a, Seyed-Yagoobi et al. 1989b). Combining two promising scalable pumping mechanisms – EHD with nozzle-diffuser elements and vibrating diaphragm actuation – Singhal and Garimella devised a micropump with the potential for direct integration into an active chip for heat removal (Singhal and Garimella 2005a, Singhal and Garimella 2005b, Singhal and Garimella 2007). A force density approach, which can predict the

induced charge density as a function of both space and time, was used in developing a numerical model of the pumping scheme such that the transient nature of traveling-wave induction EHD could be simulated (*i.e.*, charge induction, relaxation, and flow initiation). Temperature field-controlled induction EHD, in which the temperature gradient is controlled using Peltier elements, has also been discussed (Felten et al. 2006). Flow velocities were shown to increase by increasing the temperature-dependent conductivity gradient for relatively low applied voltages. Numerical schemes have been presented for traveling wave-induced electrothermal fluid flows in which material selection and device geometry play an important role in driving forces (Perch-Nielsen et al. 2004). Similar traveling wave devices, used for dielectrophoresis with conductive fluids, can result in Joule heating and temperature gradients where electrohydrodynamic forces become significant when driven at frequencies equal to the charge relaxation frequency. Illumination methods for experimental characterization of electrothermal flows can also contribute to temperature gradients and affect results (Green et al. 2001).

Early analytical models have represented the sinusoidally varying voltage at the boundary as a perfect sinusoid (Melcher and Firebaugh 1967). Subsequent numerical models have typically been validated by comparison against these early analytical models. However, practical implementations of this pumping scheme (as well as numerical model domains) necessitate a discretization of the voltage boundary. In the present work, we consider the impact of the use of such discretized electrode arrays on flow rate in traveling-wave induction EHD pumps. The performance achievable with these discrete electrodes is compared to that obtained with the ideal case of a truly sinusoidal voltage boundary condition. Optimization of the respective lengths of the electrode and the inter-electrode spacing as well as the number of phases used for actuation is explored to increase the flow rate for a given wavelength and dielectric material. We also discuss fluid selection considerations and provide flow rates that can be achieved using a range of fluid types.

2. EHD PUMPING CAPABILITY

EHD pumping has progressively found favor in applications where integration is paramount. Past induction EHD studies typically include dielectric fluids (Bohinsky and

Seyed-Yagoobi 1990) along with selected organic fluids (Crowley et al. 1990). Here, we provide a comparison of dielectric fluids (common to the electronics industry) and some common electrolyte solutions (common to the biological community) using the analytical treatment developed by Melcher and Firebaugh (Melcher and Firebaugh 1967). An approach of this type could easily be adapted to evaluate fluids specific to other applications.

2.1 Analytical treatment

Induction EHD pumping is generated through the interaction of an electric field with charges induced in the fluid medium. Induction of charge in the bulk of a liquid occurs in the presence of a gradient in the temperature (and corresponding electrical conductivity) of the liquid through anisotropic heating. These charges can then be attracted or repelled by a traveling-wave potential established on the boundary of the channel so that the fluid moves with the charges due to viscous drag (see Figure 1). Melcher and Firebaugh presented a 2D analytical solution of the velocity profile for this pumping mechanism (Melcher and Firebaugh 1967). Some important limiting assumptions of their model are as follows: effects of charge transport by the fluid are small, the gradient of the electrical conductivity is uniform (linear), and the traveling wave period is small so that thermal relaxation can be neglected (resulting in a constant temperature profile) and a time-averaged electric stress can be used. Under these assumptions, the velocity profile is described by equation 18 in their paper. If we further assume that the viscosity is uniform throughout the channel, the viscosity can be removed from the integration terms and the velocity profile easily evaluated numerically.

2.2 Working fluid considerations

Using the 2D velocity profile of Melcher and Firebaugh, we compare the fluid flows generated for several electrolytic fluids. Each set of conditions is numerically integrated using equation 18 from their paper with the additional assumption of constant viscosity (Melcher and Firebaugh 1967). Table I lists the dimensions and parameters common to the cases that will be considered in the comparisons. A wavelength of 54 μm was also used for all fluid comparison calculations of this section. We select a 10°C temperature

difference across the channel depth for all cases; alternatively, this comparison could be conducted for a given imposed heat flux. For the 10°C temperature difference assumed here, the corresponding heat flux through a water layer of thickness 50 μm ($k_{f,w}$ = 0.6 W/m·K) would be approximately 12 W/cm^2, neglecting convective effects.

Fluid properties play an important role in determining EHD pump operating conditions. The induced charge relaxation time τ is characterized by the permittivity ε and electrical conductivity σ of the fluid as $\tau = \varepsilon/\sigma$. Ideally, the traveling wave frequency should correspond to the charge relaxation time ($f_{ideal} = 1/2\pi\tau$) such that the charges are able to fully transit from one electrode to the next, without long residence times before the voltages assigned to the electrode array change. If the frequency is much lower, induced charges reach their equilibrium position opposite the traveling wave quickly and the tangential shear exerted on the fluid is small. At high frequencies, the relaxation process inhibits charge from accumulating at the surface, again reducing the shear stress (Crowley 1980).

Table II lists important properties for several electrolytic fluids. Electrolytes are commonly used in EHD studies with properties tailored by the level of doping in the aqueous solution. A range of doping molarities are listed for both KCl and NaCl with accompanying electrical properties. As a comparison, water is also included in Table II. Unless otherwise noted, electrical conductivity values were obtained using a temperature coefficient (α) and the following relation based on a known conductivity (σ) at a reference temperature, T_0 (Fuhr et al. 1992).

$$\sigma(T) = \sigma(T_0)\left[1 + \alpha(T - T_0)\right] \tag{1}$$

For the electrolyte solutions, temperature coefficients depend on the doping concentration, with higher coefficients for lower doping. However, this change is relatively small. Temperature coeffcients can play a significant role in changing the conductivity gradient and corresponding velocities. Further, as doping increases, the electrical conductivity increases and the dielectric constant decreases. Thus for higher concentration solutions, the charge relaxation time significantly decreases and optimum traveling frequencies extend well into the MHz range. Using the average velocity at the ideal frequency as the basis for comparison (Table II), we see that with increasing doping

concentration of KCl and NaCl, the average velocity decreases slightly. While the decrease in velocity does not appear to be significant, the ideal frequency of the traveling wave does increase considerably to accommodate the increase in electrical conductivity.

One possible unit of fluid comparison that emerges from Melcher and Firebaugh's analysis is the term $\varepsilon\Delta\sigma/\mu\sigma_{avg}$, where μ is the fluid viscosity. For electrolytes, this value does not vary by orders of magnitude, thereby resulting in comparable pumping velocities (despite changes in frequency). However, when the temperature coefficient varies significantly from fluid to fluid it can result in significantly different velocities at a given fluid's ideal frequency.

High concentration electrolyte solutions have the potential of causing significant Joule heating and have been excluded from the calculations. However, in some instances Joule heating may be used as the primary mechanism for establishing the temperature gradient for induction electrohydrodynamics when heat removal is not necessarily the target application. For use in biological fluid systems, the standard 0.01 M phosphate buffered saline (PBS) commonly used as a biological buffer (0.137 M NaCl, 0.0027 M KCl) has the potential of being driven without an external heating mechanism since Joule heating can be considerable at large voltages.

The increase of salt concentration in aqueous solution can cause a corresponding increase in the electrolysis of water. Combining Faraday's law of electrolysis (Serway et al. 2005) with the ideal gas law, it is possible to estimate the volume of gas generated from electrolysis. For the ~0.01 M aqueous solutions in Table II, electrolysis can become significant as the volume of gas generated begins to fill the pumping volume when left stagnant. However, as the liquid is pumped, the gas generated due to electrolysis would travel with the transported liquid such that buildup of gas in the pump volume could be mitigated.

3. NUMERICAL MODEL OF EHD PUMPING

To address some of the limitations of the analytical approach to modeling EHD, a transient numerical model was developed using the force-density approach that can predict the induced charge density as a function of both space and time. The geometry and boundary conditions associated with discrete electrodes are also accommodated.

A quasi-static analysis is used for modeling the induced fluid motion due to EHD, in which an electrostatic field is applied to a fluid containing electrically charged particles. The continuity equation takes the standard incompressible form with velocity v,

$$\vec{\nabla}\cdot\vec{v}=0\,. \tag{2}$$

The incompressible Navier-Stokes equation for conservation of momentum is modified to account for Coulomb forces acting on the charged particles in the fluid

$$\rho\left(\frac{\partial\vec{v}}{\partial t}+\vec{v}\cdot\vec{\nabla}\vec{v}\right)=-\vec{\nabla}p+\left(\vec{\nabla}\cdot\vec{\tau}_{ij}\right)+\vec{F}_b+q\vec{E} \tag{3}$$

in which ρ is density, p is pressure, τ is shear stress and F_b is body force. The electrostatic field $\vec{E}$ is given by

$$\vec{E}=-\vec{\nabla}\phi\,. \tag{4}$$

Gauss's law may be used to relate the electric potential ϕ to the charge density q,

$$q=\vec{\nabla}\cdot\left(\varepsilon\vec{E}\right) \tag{5}$$

where ε is the fluid permittivity. Thus the Coulomb force is represented as:

$$q\vec{E}=(-\varepsilon\vec{\nabla}^2\phi)\cdot(-\vec{\nabla}\phi)=\varepsilon\vec{\nabla}^2\phi\cdot\vec{\nabla}\phi\,. \tag{6}$$

Assuming no species reactions, conservation of charge takes the form,

$$\frac{\partial q}{\partial t}+\vec{\nabla}\cdot\vec{J}=0 \tag{7}$$

where the current density $\vec{J}$ is comprised of conduction, convection, and diffusion of charge (diffusivity D), as

$$\vec{J}=\sigma\vec{E}+q\vec{v}-D\vec{\nabla}q\,. \tag{8}$$

The resulting fluid transport equations are given below for an incompressible fluid after incorporating the Coulomb forces and neglecting body forces.

Conservation of mass:

$$\vec{\nabla}\cdot\vec{v}=0 \tag{9}$$

Conservation of momentum:

$$\rho\left(\frac{\partial\vec{v}}{\partial t}+\vec{v}\cdot\vec{\nabla}\vec{v}\right)=-\vec{\nabla}p+\left(\vec{\nabla}\cdot\tau_{ij}\right)+\varepsilon\vec{\nabla}^2\phi\cdot\vec{\nabla}\phi \tag{10}$$

Conservation of charge:

$$\frac{\partial q}{\partial t} + \vec{\nabla} \cdot \left(q\vec{v} \right) = \vec{\nabla} \cdot \left(\sigma \vec{\nabla} \phi + D \vec{\nabla} q \right) \tag{11}$$

The finite element software package FIDAP (Fluent 1998) was used to numerically model these transport equations. At each time step the voltage assigned to discrete electrodes along the boundary (used to provide a spatially varying, sinusoidal voltage along the wall) is updated using user-defined functions. Discretization of the boundary is discussed in more detail in sections that follow. The magnitude of the assigned voltage varies sinusoidally with time and with neighboring electrodes offset in time. The neighboring electrode phase shift depends on the number of electrodes used to represent the spatially varying, sinusoidal voltage. Thus, the voltage at the neighboring electrodes varies continuously in time providing a traveling wave with the neighboring, phase-shifted electrodes. Both voltage and charge distributions are tracked throughout the calculation in response to the changing voltage boundary condition. Figure 2 illustrates these boundary conditions and computational domain for a 3-phase, repulsion-type, induction EHD device.

A zero pressure gradient condition is imposed at the inlet and outlet and a subroutine was used to define and apply the traveling-wave voltage boundary condition. The voltage and velocity distributions in the fluid are initially set to zero for transient startup and application of the boundary conditions. An imposed temperature difference is applied at the upper and lower channel walls. With the top and bottom walls at a uniform temperature, the temperature field must be fully developed, in which case the energy equation reduces to a linear temperature profile. Viscous dissipation can be neglected since $\mathrm{Pr} \cdot \mathrm{Ec} \ll 1$. The temperature-dependent conductivity varies through the channel depth in a linear fashion (see also equation 1). While permittivity also varies with temperature, we have neglected permittivity variation in the aqueous solution used here since $\frac{1}{\varepsilon}\left(\frac{\partial \varepsilon}{\partial T}\right)$ is roughly 0.4% K^{-1} and $\frac{1}{\sigma}\left(\frac{\partial \sigma}{\partial T}\right)$ is roughly 2.2% K^{-1} (Green et al. 2001, Lide 2001, Perch-Nielsen et al. 2004). Further discussion of the validation of this model is provided in (Singhal and Garimella 2005b).

4. TREATMENT OF DISCRETE ELECTRODES

In electrohydrodynamic devices that incorporate a traveling-wave voltage boundary condition, the manner in which the voltage is treated in the model has a significant impact on the behavior of the fluid flow. A true sinusoidal voltage condition cannot be achieved at the boundary in practice. In order to fabricate a boundary used to provide a sinusoidally varying voltage, an ideal sinusoid must be discretized into a number of neighboring electrodes with separately assigned voltages; in addition, to avoid shorting, these neighboring electrodes must be isolated from one another. The resulting boundary condition therefore has important differences compared to an ideal sinusoidal voltage condition.

The basic design considered here is that of a wide, flat channel with electrodes placed on the underside of the top wall of the channel. Further, the electrodes cover the entire width and length of the channel. While the presence of electrodes on only one side of the channel renders the domain three-dimensional, 3D models are computationally prohibitive since very small node spacings are required to resolve the short wavelengths present in microscale devices. In the following computations, we assume a 2D representation of a 50 μm deep, 0.8 cm wide, and 1.0008 cm long channel, in view of the large channel width-to-depth ratio. A linear temperature profile is assumed through the channel depth. For all subsequent numerical calculations, the first electrolytic solution listed in Table II (2.2×10^{-5} M KCl (1)) is used at a driving voltage of 200 V. This fluid is characterized by an average conductivity of 5.43×10^{-4} S/m and dielectric constant of 80 resulting in a charge relaxation time and frequency of 1.30 μs and 122 kHz, respectively. For a driving voltage of 200 V, the temperature rise due to Joule heating can be shown to be minimal using the scaling approach outlined by Ramos et al., but without neglecting convection effects (Ramos et al. 1998). Electrolysis can also be shown to be minimal using the approach suggested in section 2.2.

In attraction-type induction EHD, the fluid at the lowest temperature which has the lowest electrical conductivity is closer to the electrodes where the most intense electric field is present in the microchannel (see Figure 1a). The fluid follows the traveling potential wave in the same direction as the induced charges are “attracted” towards the

traveling wave. In the case of repulsion-type induction EHD, the region of high electrical conductivity also has a high electric field resulting in charges being repelled in a direction opposite to that of the traveling wave (see Figure 1b). In the computations here, we consider repulsion-type EHD; the computed velocities would be essentially the same for attraction-type EHD as well. Increasing the node count from 70,749 to 129,129 resulted in a difference of less than 5% in the velocity, providing satisfactory mesh independence. Therefore, the coarser mesh was used in the following computations.

Figure 3 illustrates three possible ways in which the sinusoidal boundary condition may be approximated. First, an idealized sinusoid may be used in which each node along the boundary is assigned a voltage corresponding to $V(x) = \sin(2\pi x/\lambda)$. In this configuration, neighboring electrodes are assumed to operate without any electrical interference between neighbors. Such a condition is not achievable in practice since there would need to be some isolation between neighboring electrodes in a real device. The remaining two curves represented in Figure 3 illustrate isolation of neighboring electrodes with a dielectric for 3-phase representations of a sine curve using a zero voltage and zero voltage flux (normal to the wall) boundary condition.

4.1 Idealized-sinusoid boundary

Consider first a microscale repulsion EHD case where the voltage boundary condition is modeled using a discretized sine wave with no spacing between electrodes. As the number of nodes increases, this boundary condition approaches the perfect sinusoid condition commonly used in analytical models. The idealized-sinusoid boundary condition is produced using 36 electrodes of 1.5 microns width for a total wavelength of 54 μm (case 1 in Table III). The entire potential wave is divided into 36 phases with a different voltage applied to each phase/electrode. The voltage is then updated at each time step to achieve a traveling potential wave.

The difference in the velocity profiles resulting from the perfect sinusoid boundary condition from Melcher and Firebaugh's model and the idealized-sinusoid boundary condition using the current model (case 1, Table III) is shown in Figure 4. Integrating these profiles and dividing by the depth we obtain an average velocity of 1.79 m/s for the analytical result and 1.66 m/s for numerical case 1, for a difference of 7%.

Melcher and Firebaugh's model is designed for re-entrant channel geometries and limited to steady solutions by using a time-averaged, electric shear stress. Using the force-density approach, the current numerical model is capable of re-entrant geometries or non-zero pressure gradient scenarios. The model can predict the induced charge density as a function of both space and time, thus capturing flow transients due to induction EHD. Moreover, the effect of different voltage profiles, as well as of the presence of separate electrodes, can be considered in the present model. Unlike Melcher and Firebaugh, convection of charge is also taken into account. The finely discretized traveling wave used in our numerical results, although approaching a perfect sinusoidal condition, is also expected to have some deviation from the analytical solution with a sinusoidal boundary condition.

The simplified version of the analytical solution presented by Melcher and Firebaugh further assumes that the wavelength is much larger than the channel depth. This length-scale limitation in the analytical model and postulation about the variation of the potential and charge field profiles within the fluid make the current numerical model (using a force-density approach) applicable to a wider range of device modeling.

However, neither a perfect sinusoid nor the idealized sinusoid of case 1 can be experimentally achieved. Fabrication of such devices requires electrical isolation between neighboring electrodes at different potentials. Therefore, in practice, further relaxation of the sinusoidal boundary condition assumption is necessary.

4.2 Discretized-sinusoid boundary with isolation

In a real traveling-wave device, neighboring electrodes are electrically isolated from each other using dielectric films and/or substrates. For the same wavelength, inclusion of isolation regions in the boundary effectively reduces the electrode coverage area and density as compared to the idealized sinusoid of case 1. Two possible choices for the boundary condition in the spacing region between electrodes can be considered. Either the voltage can be set to zero, or the flux of voltage normal to the boundary ($dV/dy\big|_{wall} = -\vec{E}_y = 0$) can be set to zero. The former condition implies that there is an immediate transition to ground state beyond the electrode region, while the latter condition allows a gradual transition in voltage from one electrode to the next in the *x*

direction but restricts any voltage gradient in the *y* direction. The zero voltage flux condition results in a boundary condition that is more like an ideal sinusoid wave than the zero voltage isolation condition, and also more closely resembles a practical realization of the boundary comprised of a dielectric material. The only possible means of achieving the alternate zero voltage spacing condition would be to insert ground electrodes between the sinusoidally varying driving electrodes. However this is impractical and would also increase the total wavelength since the driving and ground electrodes would still need isolation spacing between them.

Figure 5 compares the idealized-sinusoid boundary condition (case 1) with the 3-phase (cases 2-6) and 5-phase (case 7) traveling-wave conditions that include isolation regions between electrodes and represents the transient startup response after pump activation through quasi-steady state conditions. First, consider the comparison of a 3-phase sinusoid in which 6 μm electrodes are separated by 12 μm isolation spacings (cases 2-3) to the idealized-sinusoid boundary condition (case 1). With the voltage between electrodes held to zero for the zero-voltage isolation (case 2), the magnitude of the average potential (voltage per unit area) at the top wall of the channel is significantly reduced, resulting in much smaller flow rates. For the zero voltage flux (case 3), the transition in voltage from one electrode to the next yields a larger average potential at the channel top wall, thus increasing charge induction and fluid transport. This is illustrated by the comparison provided in the voltage contour plots of Figure 6a and b for the 36-phase boundary condition (case 1) and the 3-phase, zero flux inter-electrode spacing boundary condition (case 3). At a given location in the depth of the channel, the magnitude of the voltage and corresponding electric field are clearly lower for the 3-phase cases.

4.3 Electrode coverage and density

To modify the electric field so that high volume flow rates can be achieved for the same total area available for EHD induction, either the voltage can be increased or the electrode spacing decreased; both are different approaches for increasing the electric field. In practice, there is a limit to the reduction in spacing at a given operating voltage that can be achieved between neighboring electrodes while still isolating them using a dielectric

material. Clearly, this limit is dependent on the breakdown electric field of the dielectric material used for isolation and for the fluid. Consider cases 3-5 in Table III and Figure 5. Here the wavelength is held constant but the fraction of the surface area that is covered with electrodes (electrode coverage area) is varied for the same operating conditions. The result is that for wider electrodes in the same three-phase system, the flow rate is effectively increased. The total electrode coverage area is increased by decreasing the total spacing area, resulting in an increased magnitude of the voltage experienced through the depth of the channel. Specifically, by widening the electrodes from 3 to 6 μm while keeping the pitch constant at 18 μm, the electrode coverage area increases by 16.7% but results in a 41.8% increase in flow rate. The increase appears to be roughly linear with coverage area for a total increase of 78.2% when the electrode width is increased from 3 to 9 μm. Of course, breakdown of the dielectric or fluid due to the presence of very high electric fields would limit the extent to which the electrode width can be increased at a fixed wavelength. Similarly, Joule heating or electrolysis (for aqueous solutions) must also be considered with an increase in electric field strength.

Another means for increasing the electric field is simply by reducing the wavelength of the traveling wave while keeping the assigned electrode voltage magnitudes constant. Case 6 is characterized by an electrode width of 6 μm and spacing of 9 μm for a wavelength of 45 μm. Compared to case 3, which has a longer wavelength but the same electrode width, an increase of 17.6% in net flow rate is observed in Figure 5. The increase can be attributed to the denser packing of electrodes yielding greater total electrode coverage area. The case 6 flow rate with a 40% coverage area clearly falls between the results for the 33% coverage in case 3 and the 50% coverage in case 5.

4.4 Phase representation

As seen in Figure 5, the idealized-sinusoidal voltage boundary condition at the wall produces a much higher flow rate than do the three-phase cases 2-6. One difference from case 1 is that cases 2-6 have a decreased potential in the inter-electrode spacing region. Another difference is the phase representation of the 36-phase design of case 1. While designs that exclude spacing between electrodes (as in the idealized-sinusoid case 1) are not experimentally achievable since electrical isolation between electrodes is required, the

electrode design can be modified to bring about a more symmetric and sinusoidal potential at the boundary.

Numerical case 7 (Table III) has a 5-phase electrode configuration with 6 μm electrodes and 6 μm spacing. The 60 μm wavelength in this case is slightly larger than the 54 μm for cases 1-5; however, the electrode coverage area is the same as that for case 5 (50%). Despite the coverage area being identical to that in case 5, the distribution of the assigned potential is such that the boundary more closely approximates a sinusoidal condition in case 7 and the flow rate is increased. This is evident in the comparison of the voltage contour plot for case 7 (Figure 6c) with that for the 36-phase, idealized-sinusoid (Figure 6a). Further, comparison with the 3-phase case (Figure 6b) reveals that the additional two phases significantly alter the magnitude and distribution of the voltage field. Of particular note is the fact that even though case 7 has a slightly larger wavelength (which would decrease the flow rate for the same frequency), the more sinusoidal-like boundary condition has a more profound effect on the velocity than that observed by simply changing the coverage area. For the same coverage area, the flow rate increases 73.4% from case 5 to case 7 by redistributing the electrode coverage area to approach a more symmetric boundary condition by employing a higher phase representation at the boundary.

5. CONCLUSION

Electrohydrodynamic pumping scales favorably as device size is reduced and may provide a viable option for fluid delivery mechanisms in electronics cooling or biomedical devices. The achievable flow rate can be increased through working fluid selection, device scaling, and increased electrode density, as well as by assigning electrode potentials in such a way as to approach a symmetric, sinusoidal boundary condition. Flow rate appears to increase roughly linearly with an increase in electrode coverage area. Further, by using five phases instead of three to represent the sinusoidal traveling wave (for the same coverage area), an increase in flow rate of approximately 73.4% is observed. For applications in which the anisotropic heating is a part of the device environment (as in the case of electronics cooling), the energy required for establishing the required temperature gradient across the liquid layer would not add to the

power required for device operation.

ACKNOWLEDGEMENTS

The authors gratefully acknowledge funding and support from the National Science Foundation, the industry members of the Cooling Technologies Research Center, an NSF I/UCRC, and the Indiana 21st Century Research and Technology Fund.

REFERENCES

Andersson H, Van den Berg A (2003) Microfluidic devices for cellomics: A review. Sensors and Actuators, B: Chemical 92(3):315

Barthel J, Buchner R, Munsterer M (1995) Electrolyte data collection Part 2: Dielectric properties of water and aqueous electrolyte solutions. vol. XII, DECHEMA, Frankfurt

Bohinsky BJ, Seyed-Yagoobi J (1990) Induction electrohydrodynamic pumping - Selecting an optimum working fluid. In: IEEE Industry Applications Society (IAS) Annual Meeting, Seattle, WA, October 7-12, 1990, pp. 795-801

Choi JW, Kim YK (1995) Micro electrohydrodynamic pump driven by traveling electric fields. In: IEEE Industry Applications Conference, Thirtieth IAS Annual Meeting, Orlando, Florida, October 8-12, 1995, vol. 2, pp. 1480-1484

Crowley JM (1980) The efficiency of electrohydrodynamic pumps in the attraction mode. Journal of Electrostatics 8(2-3):171-181

Crowley JM, Wright GS, Chato JC (1990) Selecting a working fluid to increase the efficiency and flow rate of an EHD pump. IEEE Transactions on Industry Applications 26(1):42-49

Felten M, Geggier P, Jager M, Duschl C (2006) Controlling electrohydrodynamic pumping in microchannels through defined temperature fields. Physics of Fluids 18(5):051707

Fluent (1998) FIDAP 8.7.4, finite element software

Fu AY, Chou HP, Spence C, Arnold FH, Quake SR (2002) An integrated microfabricated cell sorter. Anal. Chem. 74(11):2451-2457

Fu AY, Spence C, Scherer A, Arnold FH, Quake SR (1999) A microfabricated fluorescence-activated cell sorter. Nature Biotechnol. 17:1109-1111

Fuhr G, Hagedorn R, Muller T, Benecke W, Wagner B (1992) Microfabricated electrohydrodynamic (EHD) pumps for liquids of higher conductivity. Journal of Microelectromechanical Systems 1(3):141-146

Fuhr G, Schnelle T, Wagner B (1994) Travelling wave-driven microfabricated electrohydrodynamic pumps for liquids. Journal of Micromechanics and Microengineering 4(4):217-226

Garimella SV, Singhal V, Liu D (2006) On-chip thermal management with microchannel heat sinks and integrated micropumps. Proceedings of the IEEE 94(8):1534-1548

Green NG, Ramos A, Gonzalez A, Castellanos A, Morgan H (2001) Electrothermally induced fluid flow on microelectrodes. Journal of Electrostatics 53(2):71-87

Horiba (2008) The Story of Conductivity: Temperature Compensation in http://www.jp.horiba.com/story_e/conductivity/conductivity_04.htm, accessed March 17, 2008

Iverson BD, Garimella SV (2008) Recent advances in microscale pumping technologies: a review and evaluation. Microfluidics and Nanofluidics Available online DOI 10.1007/s10404-008-0266-8

Janssen LPBM, Warmoeskerken MMCG (1987) Transport phenomena data companion, Edward Arnold, London

Laser DJ, Santiago JG (2004) A review of micropumps. Journal of Micromechanics and Microengineering 14(6):35-64

Lide D (2001) CRC Handbook of Chemistry and Physics, 82 ed, CRC Press, New York

Mahajan R, Chiu C-P, Chrysler G (2006) Cooling a microprocessor chip. Proceedings of the IEEE 94(8):1476-1486

Melcher JR (1966) Traveling-wave induced electroconvection. Physics of Fluids 9(8):1548-1555

Melcher JR, Firebaugh MS (1967) Traveling-wave bulk electroconvection induced across temperature gradient. Physics of Fluids 10(6):1178-1185

Perch-Nielsen IR, Green NG, Wolff A (2004) Numerical simulation of travelling wave induced electrothermal fluid flow. Journal of Physics D: Applied Physics 37(16):2323-2330

Ramos A, Morgan H, Green NG, Castellanos A (1998) AC electrokinetics: A review of forces in microelectrode structures. Journal of Physics D: Applied Physics 31(18):2338-2353

Serway RA, Moses CJ, Moyer CA (2005) Modern Physics, 3rd ed, Brooks Cole, Belmont, MA

Seyed-Yagoobi J (2005) Electrohydrodynamic pumping of dielectric liquids. Journal of Electrostatics 63(6-10):861-869

Seyed-Yagoobi J, Chato JC, Crowley JM, Krein PT (1989a) Induction electrohydrodynamic pump in a vertical configuration: Part 1. Theory. Journal of Heat Transfer 111(3):664-669

Seyed-Yagoobi J, Chato JC, Crowley JM, Krein PT (1989b) Induction electrohydrodynamic pump in a vertical configuration: Part 2. Experimental study. Journal of Heat Transfer 111(3):670-674

Singhal V, Garimella SV (2005a) Influence of bulk fluid velocity on the efficiency of electrohydrodynamic pumping. Journal of Fluids Engineering 127(3):484-494

Singhal V, Garimella SV (2005b) A novel valveless micropump with electrohydrodynamic enhancement for high heat flux cooling. IEEE Transactions on Advanced Packaging 28(2):216-230

Singhal V, Garimella SV (2007) Induction electrohydrodynamics micropump for high heat flux cooling. Sensors and Actuators, A: Physical 134(2):650-659

Singhal V, Garimella SV, Raman A (2004) Microscale pumping technologies for microchannel cooling systems. Applied Mechanics Reviews 57(1-6):191-221

Wolff A, Perch-Nielson IR, Larsen UD, Friis P, Goranovic G, Poulsen CR, Kutter JP, Telleman P (2003) Integrating advanced functionality in a microfabricated high-throughput fluorescent-activated cell sorter. Lab on a Chip 3:22-27

Table I. Parameters used in analytical and numerical EHD calculations.

Symbol	Property	Value
h	Channel height	50 [μm]
L	Channel length	1.0008 [cm]
ΔT	Wall temperature difference	10 [°C]
ρ	Density	987 [kg/m^3]
μ	Viscosity	5.28 x 10^{-4} [N·s/m^2]

Table II. Fluid properties and corresponding average velocities generated with representative liquids at a driving voltage of 50 V. Calculation for additional fluids can be similarly carried out following equation 18 from (Melcher and Firebaugh 1967) assuming constant viscosity.

Fluid	Temperature coefficient	Average conductivity [S/m]	Dielectric constant	Average velocity (at f_{ideal}) [cm/s]	Reference
Water	2.6 - 3.0%	1.89×10^{-5}	80	51.6	(Janssen and Warmoeskerken 1987)
2.2×10^{-5} M KCl (1)	0.82%[a]	5.43×10^{-4}	80	11.2	(Fuhr et al. 1992)
2.2×10^{-5} M KCl (2)	2.11%[b]	5.44×10^{-4}	80	24.0	(Horiba 2008)
0.013 M KCl	2.11%	0.2632	77.9	23.4	(Barthel et al. 1995, Horiba 2008, Lide 2001)
0.001 M NaCl	2.19%	0.0206	78.1	24.0	(Barthel et al. 1995, Horiba 2008, Lide 2001)
0.011 M NaCl	2.19%	0.1995	77.7	23.9	(Barthel et al. 1995, Horiba 2008, Lide 2001)

[a] Based on selected conductivity values in the range provided by (Fuhr et al. 1992)

[b] Based on extrapolated data from (Horiba 2008)

Table III. Various cases of sinusoidal voltage boundary condition and geometry for repulsion-type EHD considered in the computations at a driving voltage of 200 V

Case	Boundary condition in inter-electrode space	Number of phases	Electrode width / spacing [μm]	Wavelength [μm]
1	Idealized-sinusoid	36	1.5 / 0	54
2	Zero voltage	3	6 / 12	54
3	Zero voltage flux	3	6 / 12	54
4	Zero voltage flux	3	3 / 15	54
5	Zero voltage flux	3	9 / 9	54
6	Zero voltage flux	3	6 / 9	45
7	Zero voltage flux	5	6 / 6	60

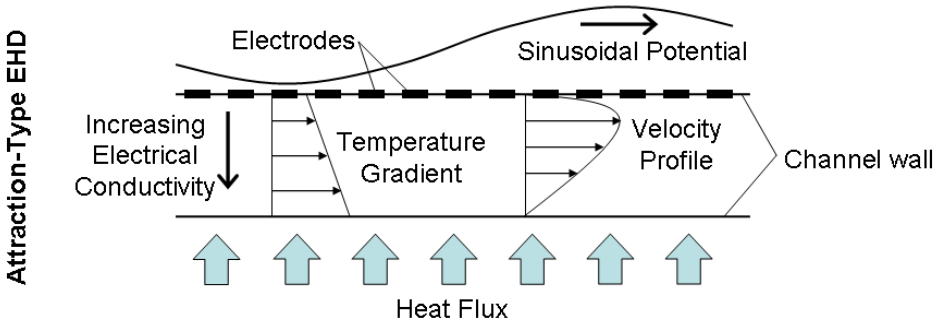

(a)

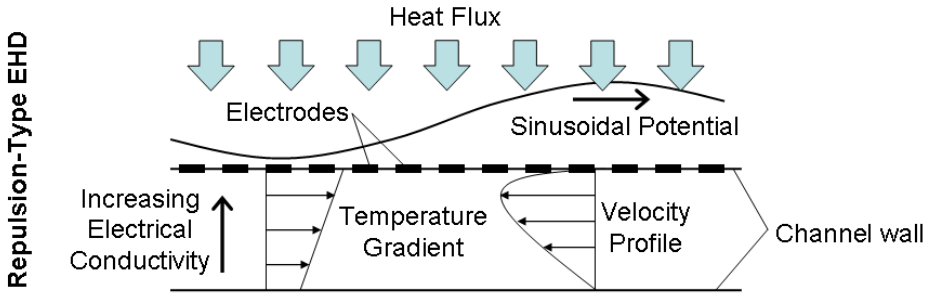

(b)

Figure 1. Schematic illustration of (a) attraction- and (b) repulsion-type induction EHD configurations for fluids in which the electrical conductivity increases with temperature.

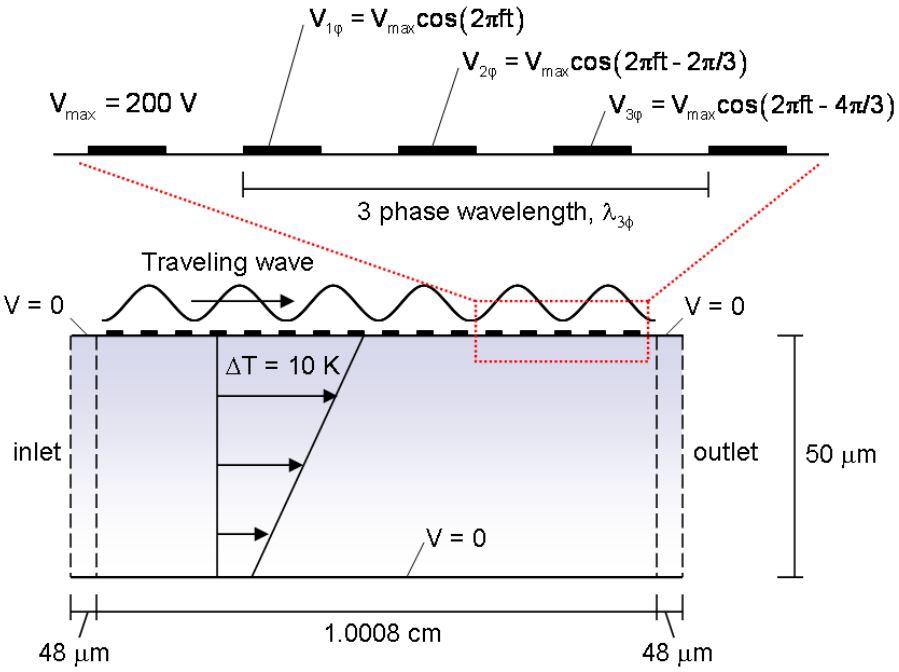

Figure 2. Computational domain for a representative 3-phase, repulsion-type, induction EHD device.

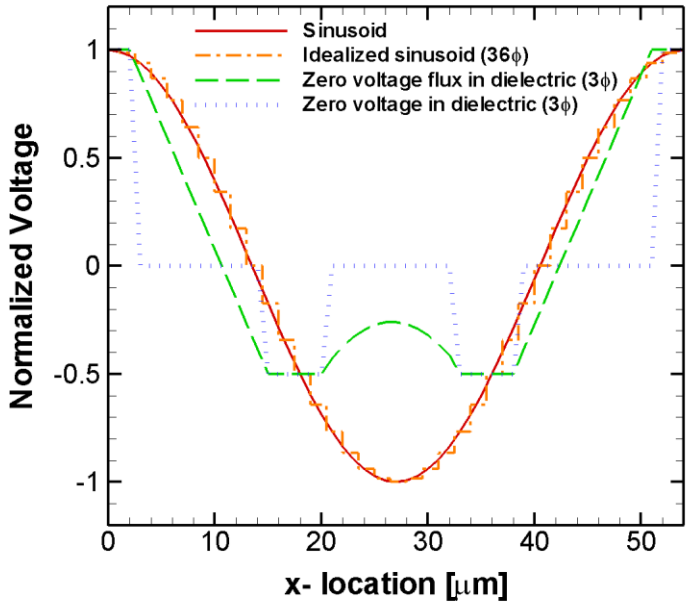

Figure 3. Approximate methods of representing an ideal, sinusoidal traveling wave (wavelength 54 μm) at an arbitrary time instant: a discretized 36-phase wave, a 3-phase wave with zero voltage boundary condition in the inter-electrode dielectric space, and a 3-phase wave with zero voltage flux boundary condition in the inter-electrode dielectric space. The curves representing 3-phase waves have 6 μm wide electrodes and 12 μm wide inter-electrode dielectric spaces. For the zero flux boundary condition, the transitions in voltage shown in the dielectric layers are purely schematic.

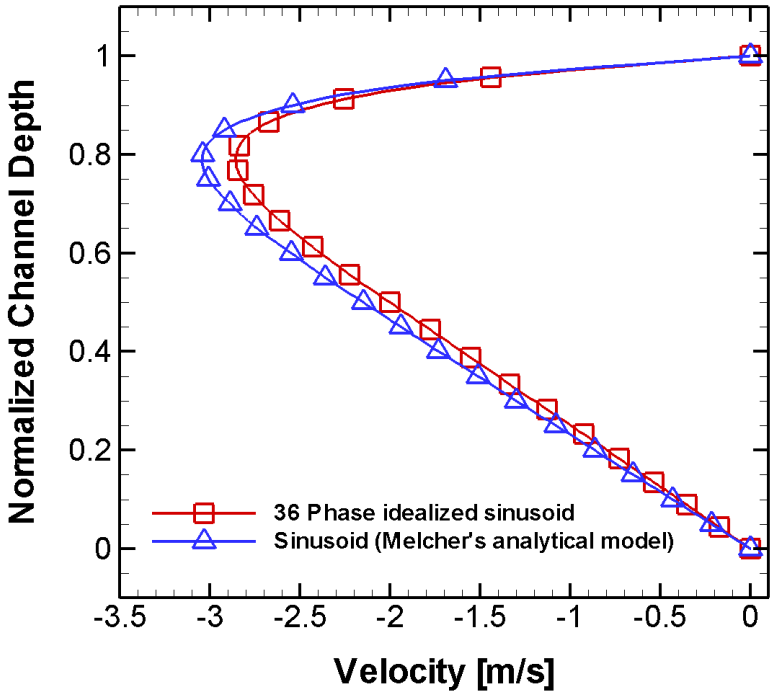

Figure 4. Comparison of Melcher's analytical result with numerical modeling results of a discretized sinusoidal potential boundary condition with 36 phases (case 1, Table III).

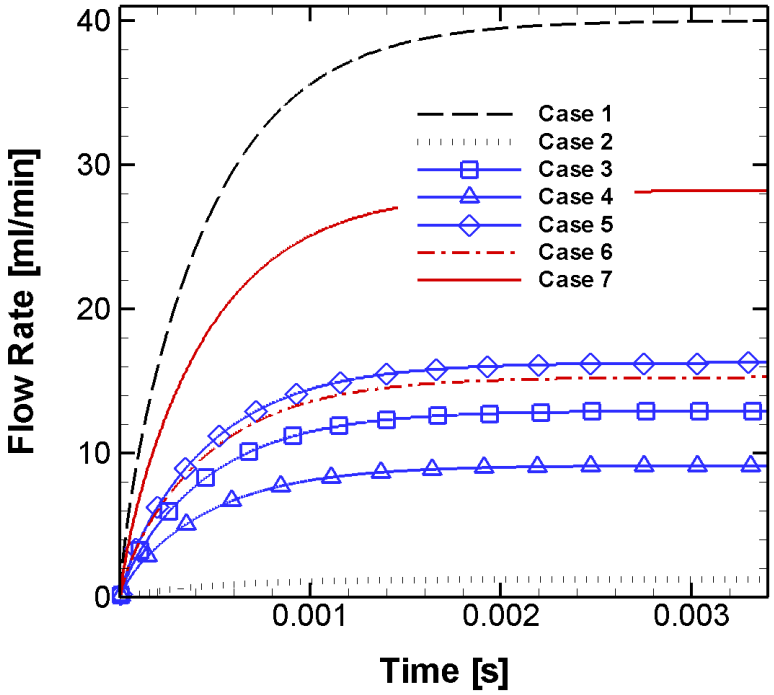

Figure 5. Calculated net flow rates for cases 1-7, Table III. Case 1 is an idealized, 36-phase sinusoid; cases 2-6 are 3-phase sinusoids; case 7 is a 5-phase sinusoid boundary condition.

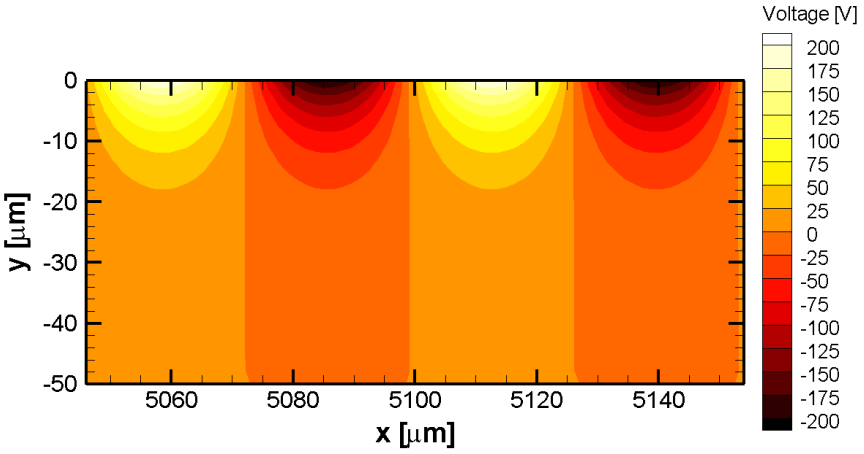

(a)

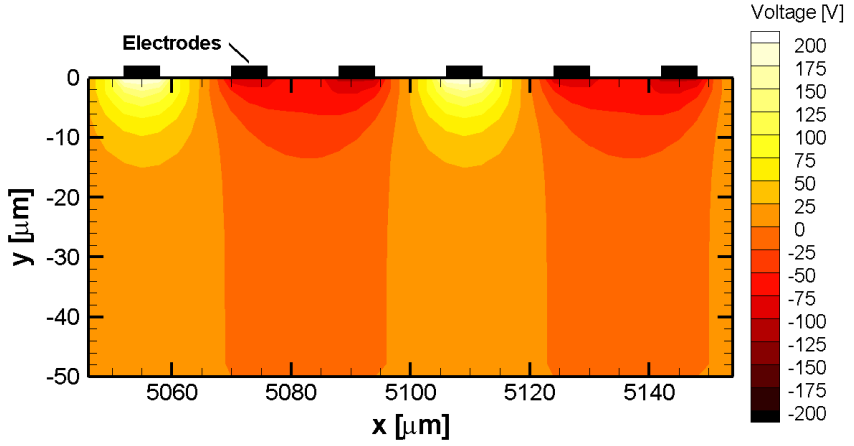

(b)

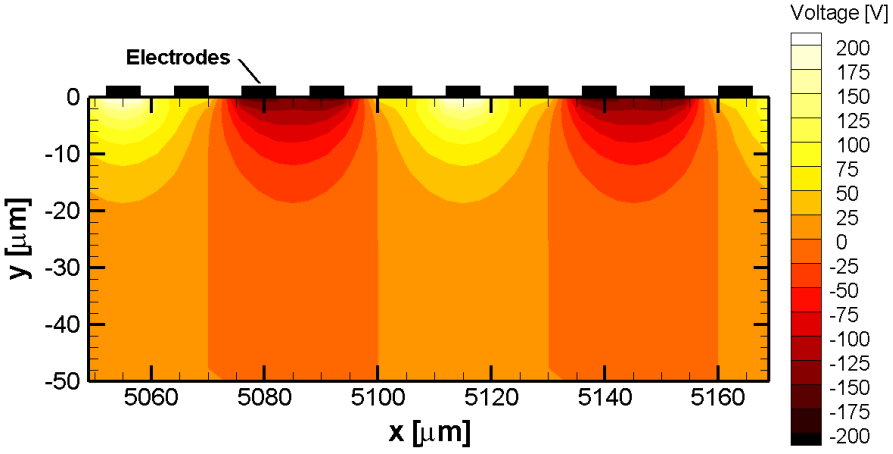

(c)

Figure 6. Voltage contour plots over a width of two wavelengths at a time corresponding to a maximum voltage of 200 V for (a) case 1 with a 36-phase, discretized boundary, (b) case 3 with a 3-phase, zero flux inter-electrode spacing, and (c) case 7 with a 5-phase, zero flux inter-electrode spacing (see also Table III).